Journal of Marine Science and Engineering

MDPI

Article

Functional Testing and Numerical Analysis of Initial Freezing in Overboard Discharge Valve at Small Lift

Peiyue Li [1], Shihao Zhou [1], Xinqi Zhang [1], Cheng Li [1], Xingyu Liu [1], Zhenhao Xiao [2,3] and Yuwei Sun [2,3,*]

[1] Luoyang Ship Material Research Institute (LSMRI), Luoyang 471000, China; lpy110015@163.com (P.L.); zhoushihao1949@163.com (S.Z.); zxq_7258@163.com (X.Z.); lutlicheng@163.com (C.L.); 04liuxingyu@163.com (X.L.)
[2] School of Naval Architecture, Ocean and Energy Power Engineering, Wuhan University of Technology, Wuhan 430063, China; x861936634@163.com
[3] State Key Laboratory of Maritime Technology and Safety, Wuhan University of Technology, Wuhan 430063, China
* Correspondence: ywsun@whut.edu.cn; Tel.: +86-186-9619-0373

Abstract

Local freezing may affect subsequent discharge when a cold fluid enters a water-containing passage in an overboard discharge valve. Compressed-air functional tests assessed prototype opening and discharge performance. A volume-of-fluid (VOF) model coupled with the enthalpy–porosity method examined initial freezing during low-flow operation at a small valve lift. The measured assembly opening pressure was 1.53×10^6 Pa. The overboard check valve discharged 0.67814–0.79061 kg·s^{-1} at 3.55×10^6–3.75×10^6 Pa. With constant gas properties, all cases were compared over 0–0.10 s. Increasing inlet mass flow from 0.0010 to 0.0020 kg·s^{-1} reduced the terminal ice-phase fraction from 0.70% to 0.14%. The time-averaged fraction decreased from 0.39% to 0.12%, with a local increase at an intermediate flow rate. Terminal and time-averaged fractions were lower at equivalent roughness of 0.6–0.7 μm. At 0.8–1.0 μm, the ice-phase fraction continued increasing near the end of the window. Within the prescribed model, these results describe how flow rate and roughness affect the initial thermal shock and phase-change history. Their scope is limited to the initial transient response and excludes predictions of steady-state ice accumulation or valve blockage.

Keywords: overboard discharge valve; functional testing; transient freezing; VOF; enthalpy–porosity method; wall roughness

Academic Editor: Pasqualino Corigliano

Received: 3 October 2026
Revised: 27 October 2026
Accepted: 30 October 2026
Published: 1 November 2026

Copyright: © 2026 by the authors. Licensee MDPI, Basel, Switzerland. This article is an open access article distributed under the terms and conditions of the Creative Commons Attribution (CC BY) license.

1. Introduction

Marine valves experience pressure loads and temperature gradients during the transport and discharge of cryogenic fluids. Local cooling can freeze residual water within their passages. Previous studies have examined heat transfer in cryogenic valves for polar vessels, icing on offshore structures, and protective measures [1–3]. Internal freezing is affected by throttling clearances, passage bends, and recirculation zones. Even before complete blockage occurs, local ice growth can alter the available flow area and near-wall heat transfer.

Flow and phase change are coupled in both directions. Convection transports heat at the phase boundary, while boundary motion changes the local velocity and temperature distributions. Recent studies have examined how natural convection, turbulent shear, and the density anomaly of water affect ice growth and melting [4–10]. Saline-water freezing

also involves salt rejection, brine concentration, and changes in freezing temperature, distinguishing it from pure-water phase change [11–13]. Assessments of internal valve freezing therefore require consideration of thermal boundaries, flow structure, and water-phase properties.

Simulations and visualization experiments on saline droplets show that salinity, substrate temperature, and surface wettability jointly affect freezing [14–16]. VOF has been coupled with immersed-boundary, enthalpy–porosity, and level-set methods to describe interface motion and freezing in liquid films and droplets [17–21].

Studies on moving cold surfaces, vertical plates, and ultra-cold substrates further show that boundary motion and interfacial dynamics affect freezing morphology and duration [22–26]. A shipboard water-injection study combined VOF and enthalpy–porosity models with scaled experiments to compare the effects of flow velocity, pipe diameter, and injection position [27]. Overboard discharge valves contain multiple throttling and transition regions. Their early-stage ice accumulation consequently requires analysis of the specific passage geometry.

Equivalent sand-grain roughness affects near-wall momentum transport through wall functions. In physical surfaces, wettability, microscopic morphology, and material properties jointly govern ice adhesion. Surface-treatment, coating, and deicing studies show no universal monotonic relationship between roughness and ice adhesion [28–37]. Numerical roughness studies should therefore focus on the associated flow and phase-change responses.

Studies of ice-slurry pipe flow, melting in flowing liquids, and cryogenic chilldown show that velocity and geometry effects depend on thermal boundaries and flow conditions [38–42]. Freezing-induced blockage and phase-change calculations also require distinction between physical-model applicability and numerical discretization error [43–45]. Evaluation metrics must match the spatial and temporal scales under investigation [46,47].

Prototype functional tests were first used to assess opening and discharge performance of the overboard discharge valve. Transient simulations at a fixed small lift then examined local freezing when a cold fluid entered the water-containing passage. The tests and simulations addressed valve operation and the initial phase-change response, respectively. The numerical study compared inlet mass flow and equivalent roughness under the same geometry and property assumptions. Terminal values, time averages, peak times, and late-stage slopes characterized freezing over 0–0.10 s. Existing records beyond this window were also used to discuss the applicability of the comparison interval.

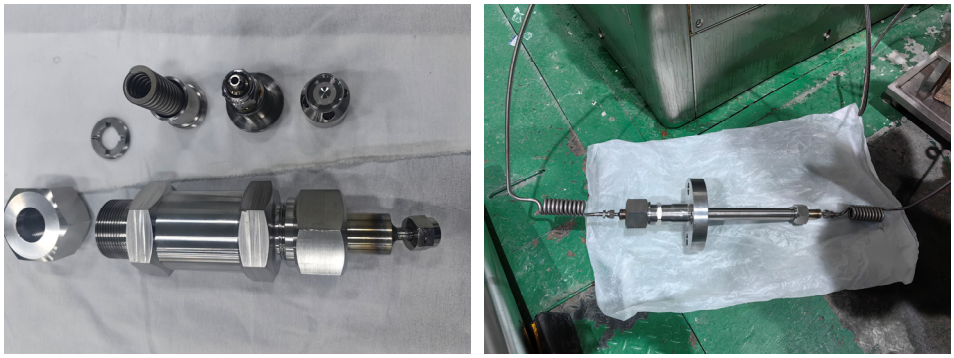
2. Prototype Functional Tests and Frost Observations

2.1. Test Specimen and Arrangement

The specimen was one ZD092BT-024-54 overboard discharge valve assembly comprising an inboard check valve, an overboard check valve, and pressure-resistant pipe fittings. Functional testing was conducted on 4 February 2026. Measurements covered the opening pressure of the assembly and both check valves, together with check-valve discharge rates at specified pressure values. The working fluid was compressed air, and the ambient temperature was 281.15–283.15 K (8–10 °C). Testing followed GB/T 12241—2021 [48] and the prototype test protocol. The measurements were taken from Report No. 2026FM099 [49].

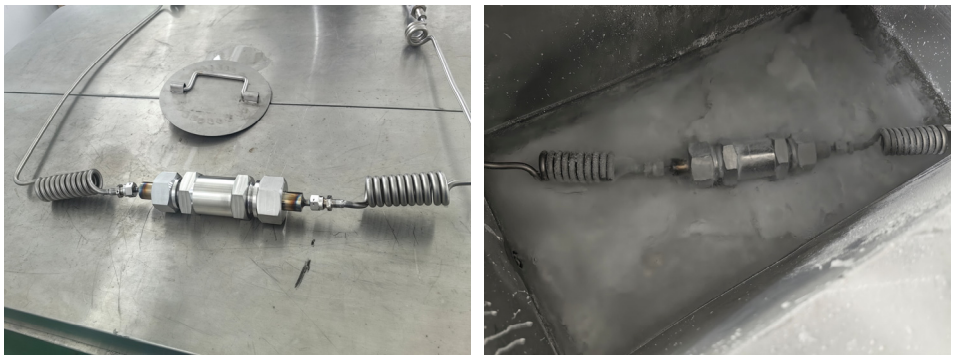
High-pressure oxygen testing requires compatible materials and dedicated protective provisions [50]. Safety constraints on low-temperature, high-pressure oxygen testing led to the use of compressed air for prototype opening and discharge tests. Local cooling during compressed-air discharge may still cause freezing in water-containing passages. Internal phase change therefore warrants examination alongside basic opening and discharge performance. For the intended application involving low-temperature oxygen,

simulations examined initial freezing after oxygen entered the water-containing passage, including the effects of inlet flow rate and wall roughness. Figure 1 shows the prototype and associated valve components. Figure 2 documents the connecting pipework and tank arrangement during cooling in October 2025, identifying the specimen locations and visible surface conditions. These images were recorded separately from the compressed-air functional tests reported in Tables 1 and 2.



(**a**) (**b**)

Figure 1. Overboard discharge valve assembly and associated components. (**a**) Valve components and disassembled parts; (**b**) flanged assembly and connecting pipework.



(**a**) (**b**)

Figure 2. Photographs of the connections and arrangement during valve cooling. (**a**) Valve components and connecting pipework; (**b**) specimen in the tank and surrounding mist.

Table 1. Opening pressure of the overboard discharge valve assembly and check valves [49].

Specimen	Opening Pressure, Pa (MPa)
Overboard discharge valve assembly	1.53×10^6 (1.53)
Inboard check valve	6.50×10^5 (0.65)
Overboard check valve	6.50×10^5 (0.65)

Table 2. Pressure and discharge mass flow rate for the two check-valve types [49].

Valve Type	Pressure, Pa (MPa)	Mass Flow Rate, kg·s^{-1}	Reported Value, kg·h^{-1}
Inboard check valve	3.55×10^6 (3.55)	0.73033	2629.2
Inboard check valve	3.65×10^6 (3.65)	0.74825	2693.7
Inboard check valve	3.70×10^6 (3.70)	0.75672	2724.2

Overboard check valve	3.55×10^6 (3.55)	0.67814	2441.3
Overboard check valve	3.60×10^6 (3.60)	0.71431	2571.5
Overboard check valve	3.75×10^6 (3.75)	0.79061	2846.2

2.2. Opening and Discharge Performance

Table 1 lists the opening pressure values of the assembly and both check valves. The assembly opened at 1.53×10^6 Pa (1.53 MPa), and both check valves opened at 6.50×10^5 Pa (0.65 MPa). These measurements confirm pressure-actuated opening under the test conditions.

Table 2 presents the discharge mass flow rates at each pressure value. The original report values in kg·h^{-1} are retained alongside conversions using 1 kg·h^{-1} = 1/3600 kg·s^{-1}.

Discharge increased with pressure over the tested range for each valve type (Figure 3). For the overboard check valve, discharge rose from 0.67814 to 0.79061 kg·s^{-1} over 3.55×10^6–3.75×10^6 Pa, an increase of 16.6%. For the inboard check valve, discharge rose from 0.73033 to 0.75672 kg·s^{-1} over 3.55×10^6–3.70×10^6 Pa, an increase of 3.6%.

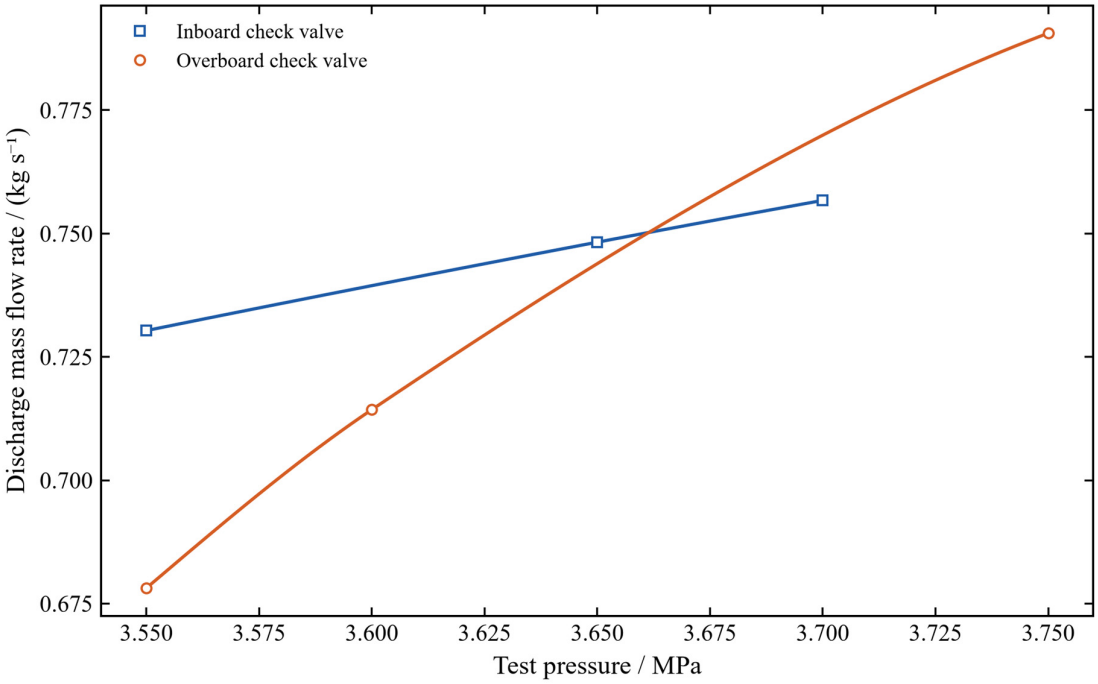


Figure 3. Pressure and discharge mass flow rate for the two check-valve types. Symbols indicate measured values; curves use shape-preserving interpolation.

2.3. Test Factors and Data Analysis

Separate linear regressions were fitted for each valve type, using upstream pressure as the independent variable and discharge mass flow rate as the response. Each group contained three pressure levels. Table 3 presents the coding and regression matrices. Because the two groups did not share all pressure levels, no interaction between pressure and valve type was estimated.

The coded pressure was defined separately for each group as $x = (p - p_c)/\Delta p$. Here, p, p_c, and Δp are in Pa, and x is dimensionless. The linear model was $\hat{m} = b_0 + b_1 x$, with $\hat{m}$,

b_0, and b_1 in kg·s^{-1}. For the inboard valve, $p_c = 3.625 \times 10^6$ Pa, and $\Delta p = 7.50 \times 10^4$ Pa. For the overboard valve, $p_c = 3.650 \times 10^6$ Pa, and $\Delta p = 1.00 \times 10^5$ Pa. The two matrix columns contain the constant 1 and x, respectively.

Table 3. Tested pressure conditions and coded regression matrices for each valve type.

Case	Valve Type	p, Pa	Constant	Coded Pressure x
I1	Inboard check valve	3.55×10^6	1	−1.000
I2	Inboard check valve	3.65×10^6	1	0.333
I3	Inboard check valve	3.70×10^6	1	1.000
O1	Overboard check valve	3.55×10^6	1	−1.000
O2	Overboard check valve	3.60×10^6	1	−0.500
O3	Overboard check valve	3.75×10^6	1	1.000

Within its tested pressure range, the fitted relationship for the inboard check valve was $\hat{m} = 0.10422 + 1.76389 \times 10^{-7} p$. The corresponding fit for the overboard check valve was $\hat{m} = -1.27057 + 5.49979 \times 10^{-7} p$. Pressure p is in Pa, predicted mass flow $\hat{m}$ is in kg·s^{-1}, and the slopes have unit kg·s^{-1}·Pa^{-1}. The intercepts are local linear-fit parameters. The equations are used only for comparisons within the corresponding tested pressure intervals. Table 4 summarizes the regression results.

Table 4. Separate linear regressions of pressure and discharge mass flow rate for the two check-valve types.

Valve Type	b_0, kg·s^{-1}	b_1, kg·s^{-1}	R^2	RMSE, kg·s^{-1}	Residual d.f.
Inboard check valve	0.743632	0.013229	0.9998	1.500×10^{-4}	1
Overboard check valve	0.736851	0.054998	0.9940	3.645×10^{-3}	1

The residual $e_i = m_i - \hat{m}_i$ has unit kg·s^{-1}. The coefficient of determination, $R^2 = 1 - \Sigma e_i^2 / \Sigma (m_i - \bar{m})^2$, is dimensionless. The root-mean-square residual, RMSE = $\sqrt{(\Sigma e_i^2 / n)}$, has unit kg·s^{-1}. Here, m_i and $\bar{m}$ are the measured mass flow rate and the within-group mean, respectively. Each group contained $n = 3$ observations and one residual degree of freedom. The respective R^2 values were 0.9998 and 0.9940. These regressions describe the pressure–discharge relationship within each tested interval.

Pressure and discharge were recorded to 0.01 MPa and 0.1 kg·h^{-1}, respectively. Under a uniform rounding model, the standard uncertainty components from recording resolution are $u_{p,r} = d_p/\sqrt{12}$ and $u_{m,r} = d_m/\sqrt{12}$. The recording increments are $d_p = 1.0 \times 10^4$ Pa and $d_m = 0.1/3600$ kg·s^{-1}. These give $u_{p,r} = 2.89 \times 10^3$ Pa and $u_{m,r} = 8.02 \times 10^{-6}$ kg·s^{-1}. These components represent recording resolution alone, rather than instrument accuracy or combined measurement uncertainty.

2.4. External Frost Observations and Research Question

Figures 2b and 4 show white frost-like deposits on the housing, fittings, and adjacent pipework, with mist surrounding the specimen in the tank. External frosting reflects valve cooling and interaction with the surrounding humid air; it does not establish the extent of freezing inside the valve. Functional testing showed that the prototype could open and discharge, whereas internal phase change following cold-fluid entry requires separate investigation. The following analysis therefore examines initial freezing at a small lift and low flow rates. The photographs provide visual observations only. They are not used for quantitative comparison with numerical results or to infer fluid temperature, flow rate, or exposure duration.



(**a**) (**b**)

Figure 4. Frost-like deposits on external valve surfaces. (**a**) Long flanged assembly; (**b**) short valve component and fittings.

3. Mathematical Model and Numerical Methods

3.1. Geometry and Computational Domain

The simulations used a fixed small-lift fluid domain with a valve-disc lift of 0.5×10^{-3} m (0.5 mm). The inlet, valve body, neck transition, throttling region, and downstream passage were retained. Bolt holes, external stiffeners, seal grooves, and small fillets were omitted. Figure 5 shows only the local structure around the valve seat and adjacent throttling passage; the extent of the computational domain was unchanged. The total domain length was 0.3846 m, and its maximum diameter was 0.0530 m. The valve-body section was 0.1146 m long, and the downstream passage diameter was 0.0270 m. The disc position remained fixed during the calculation, so passage changes caused by further disc lift were not considered.

Local mesh refinement was applied near the outer valve-body wall in region A and within the neck transition and throttling region B. The first-layer height was 1.0×10^{-5} m.

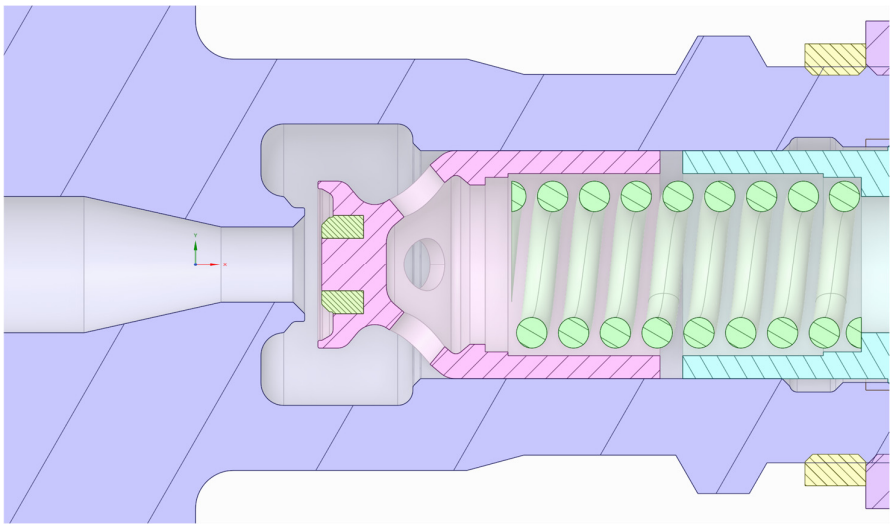


Figure 5. Local axial section through the valve seat and adjacent throttling passage at small lift. The valve-disc lift is 0.5 mm. Colors distinguish the CAD assembly components and do not represent physical-field values.

3.2. Governing Equations

3.2.1. Phase Transport and Momentum Equations

VOF tracks the interface between oxygen and the water phase, which includes liquid water and ice. Their dimensionless volume fractions are α_g and α_l, respectively. The liquid fraction within the water phase is β. Mixture density ρ (kg·m^{-3}) and dynamic viscosity μ (Pa·s) are calculated below. Subscripts g and l denote oxygen and the water phase, respectively.

$$\rho = \alpha_l \rho_l + \alpha_g \rho_g \tag{1}$$

$$\mu = \alpha_l \mu_l + \alpha_g \mu_g \tag{2}$$

The phase volume fractions satisfy

$$\alpha_g + \alpha_l = 1 \tag{3}$$

No evaporation or condensation mass transfer is prescribed between oxygen and the water phase. For the constant-density water phase, the volume-fraction transport equation is

$$\partial \alpha_l / \partial t \; + \; \nabla \cdot (\alpha_l v) \; = \; 0 \tag{4}$$

In Equation (4), t is time (s), and $\mathbf{v}$ is the velocity vector (m·s^{-1}). The local Courant number is defined as

$$\mathrm{CFL} = \frac{|\mathbf{v}| \Delta t}{\Delta x} \leq 1 \tag{5}$$

In Equation (5), Δt is the solver time step (s), Δx is the characteristic cell length (m), and CFL is dimensionless. The mixture mass and momentum equations are

$$\frac{\partial \rho}{\partial t} + \nabla \cdot (\rho \mathbf{v}) = 0 \tag{6}$$

$$\frac{\partial (\rho \mathbf{v})}{\partial t} + \nabla \cdot (\rho \mathbf{v}\mathbf{v}) = -\nabla p + \nabla \cdot \boldsymbol{\tau} + \rho \mathbf{g} + \mathbf{S}_{\mathrm{mom}} \tag{7}$$

In Equations (6) and (7), p is pressure (Pa), $\boldsymbol{\tau}$ is the stress tensor (Pa), and $\mathbf{g}$ is gravitational acceleration (m·s^{-2}). S_{mom} is the volumetric momentum resistance associated with solidification (N·m^{-3}). The wall shear stress is

$$\tau_w = \mu_{\mathrm{eff}}\left(\frac{\partial u_{\parallel}}{\partial y}\right)_{y=0} \tag{8}$$

In Equation (8), τ_w is wall shear stress (Pa), and μ_{eff} is effective viscosity (Pa·s). The quantities $u_{\parallel}$ and y are tangential velocity (m·s^{-1}) and wall-normal distance (m), respectively. The area-averaged shear stress on the boundary named wall is used to compare near-wall momentum exchange.

3.2.2. Energy Equation and Phase-Change Model

Water solidification and melting are calculated using the enthalpy–porosity method in the Fluent solidification/melting model. VOF tracks the gas–liquid interface. The total enthalpy H of the water phase comprises sensible enthalpy h and latent enthalpy βL. The quantities H, h, reference enthalpy h_{ref}, and latent heat L are in J·kg^{-1}. Temperature T and reference temperature T_{ref} are in K; specific heat at constant pressure c_p is in J·kg^{-1}·K^{-1}.

$$H = h + \beta L, h = h_{\mathrm{ref}} + \int_{T_{\mathrm{ref}}}^{T} c_p \mathrm{d}T \tag{9}$$

Neglecting the enthalpy flux caused by species diffusion, the energy equation is

$$\frac{\partial(\rho H)}{\partial t} + \nabla \cdot (\rho \mathbf{v} H) = \nabla \cdot (k_{\mathrm{eff}} \nabla T) + S_E \tag{10}$$

In Equation (10), k_{eff} is effective thermal conductivity (W·m^{-1}·K^{-1}), and S_E is the volumetric energy source (W·m^{-3}). The latent heat of fusion for oxygen is set to zero. A user-defined function (UDF) specifies the thermal conductivity of the water phase, while the built-in solver model handles phase-change source terms [51]. Table 5 lists the material properties and phase-change parameters.

Table 5. Material properties and phase-change parameters used in the simulations.

Property or Parameter	Water Phase	Oxygen
Density, kg·m^{-3}	998.2	3.136
Specific heat capacity, J·kg^{-1}·K^{-1}	4182	919.31
Thermal conductivity, W·m^{-1}·K^{-1}	0.620271 (T > 273.0 K) 2.73 (T ≤ 273.0 K)	0.0246
Latent heat of fusion, J·kg^{-1}	3.34×10^5	0
Dynamic viscosity, Pa·s	1.003×10^{-3}	1.271×10^{-5}
Solidus temperature, K	273.15	—
Liquidus temperature, K	273.15	—

The model approximates phase change as the isothermal freezing of pure water at a melting temperature T_m of 273.15 K. The liquid fraction β satisfies

$$\beta = 0\,(T < T_{\mathrm{m}});\ 0 \le \beta \le 1\,(T = T_{\mathrm{m}});\ \beta = 1\,(T > T_{\mathrm{m}}) \tag{11}$$

In Equation (11), T_m is the melting temperature (K), and β is dimensionless. At T_m, β is determined from the enthalpy balance. Both the solidus and liquidus temperatures are set to 273.15 K [5,11–13,16].

The phase-change momentum resistance is expressed as

$$S_{\mathrm{mom}} = -A_{\mathrm{mush}}\,(1 - \beta)^2 v/(\beta^3 + \delta) \tag{12}$$

In Equation (12), A_{mush} is the mushy-zone resistance coefficient (kg·m^{-3}·s^{-1}). The dimensionless small constant δ prevents division by zero. The prescribed values are A_{mush} =

1.0×10^5 kg·m^{-3}·s^{-1} and $\delta = 0.001$. As the liquid fraction decreases, this resistance term suppresses velocity in the solidifying region.

3.2.3. Turbulence and Wall Roughness

Turbulence is modeled using the realizable k–ε model with standard wall functions for near-wall treatment. Neglecting buoyancy production under constant-density conditions, the principal transport equations are

$$\partial(\rho k)/\partial t + \nabla \cdot (\rho k v) = \nabla \cdot [(\mu + \mu_t/\sigma_k)\nabla k] + G_k - \rho\varepsilon_t \quad (13)$$

$$\partial(\rho\varepsilon_t)/\partial t + \nabla \cdot (\rho\varepsilon_t v) = \nabla \cdot [(\mu + \mu_t/\sigma_\varepsilon)\nabla\varepsilon_t] + \rho C_1 S\varepsilon_t - \rho C_2 {\varepsilon_t}^2/(k + \sqrt{(\nu\varepsilon_t)}) \quad (14)$$

In Equations (13) and (14), k is turbulent kinetic energy (m^2·s^{-2}), and ε_t is its dissipation rate (m^2·s^{-3}). Turbulent viscosity μ_t is in Pa·s, and the volumetric turbulent kinetic energy production G_k is in W·m^{-3}. Kinematic viscosity is $\nu = \mu/\rho$ (m^2·s^{-1}). The mean strain-rate magnitude is $S = \sqrt{(2S_{ij}S_{ij})}$ (s^{-1}), where $S_{ij} = (\partial u_i/\partial x_j + \partial u_j/\partial x_i)/2$. Here, u_i is a velocity component (m·s^{-1}), x_i is a spatial coordinate (m), and i and j are spatial indices. The dimensionless model coefficients are $\sigma_k = 1.0$, $\sigma_\varepsilon = 1.2$, and $C_2 = 1.9$. The coefficient $C_1 = \max[0.43, \eta/(\eta + 5)]$, where $\eta = Sk/\varepsilon_t$, is also dimensionless. Turbulent viscosity is calculated as $\mu_t = \rho C_\mu k^2/\varepsilon_t$, using the variable-coefficient form of C_μ in the model [51].

The roughness height K_s enters the wall treatment through the roughness function ΔB:

$$U^+ = \frac{1}{\kappa}\ln(Ey^+) - \Delta B({K_s}^+) \quad (15)$$

In Equation (15), $U^+ = u_\parallel/u_\tau$, $y^+ = \rho u_\tau y/\mu$, and $K_s^+ = \varrho u\tau K_s/\mu$ are dimensionless. The friction velocity is $u_\tau = \sqrt{(\tau_w/\rho)}$ (m·s^{-1}). The quantities κ and E are logarithmic-law constants, ΔB is the dimensionless roughness correction, and K_s is in m. The equivalent resistance parameter K_s differs from measured R_a and does not incorporate an ice-adhesion model [28,35,37,51].

3.3. Mesh Generation and Independence Assessment

Polyhedral cells were used, with local refinement near the outer valve-body wall in region A and within the neck transition and throttling region B (Figure 6).

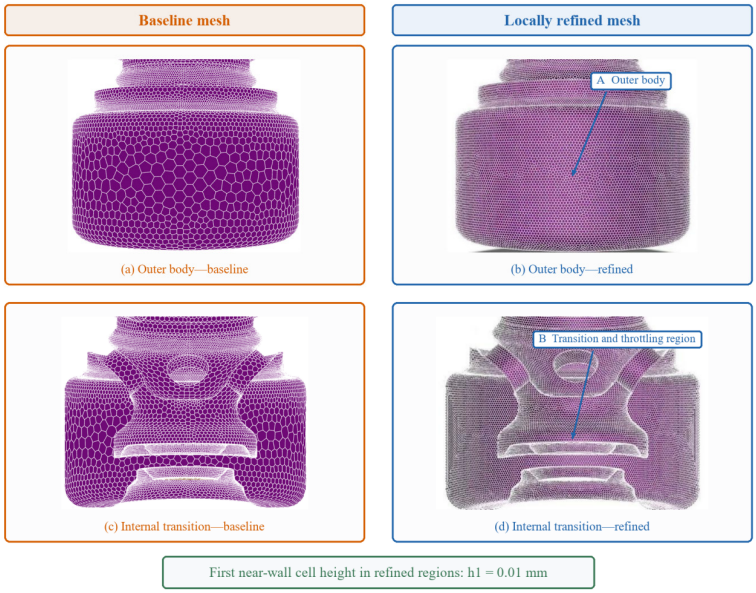


Figure 6. Base mesh and local refinement.

At an inlet mass flow rate of 0.0010 kg·s⁻¹, six meshes contained approximately 4.21, 4.82, 5.58, 6.41, 7.15, and 7.91 million cells. Local ice-phase fractions in regions A and B and the maximum velocity within the valve were compared at 0.10 s (Figure 7).

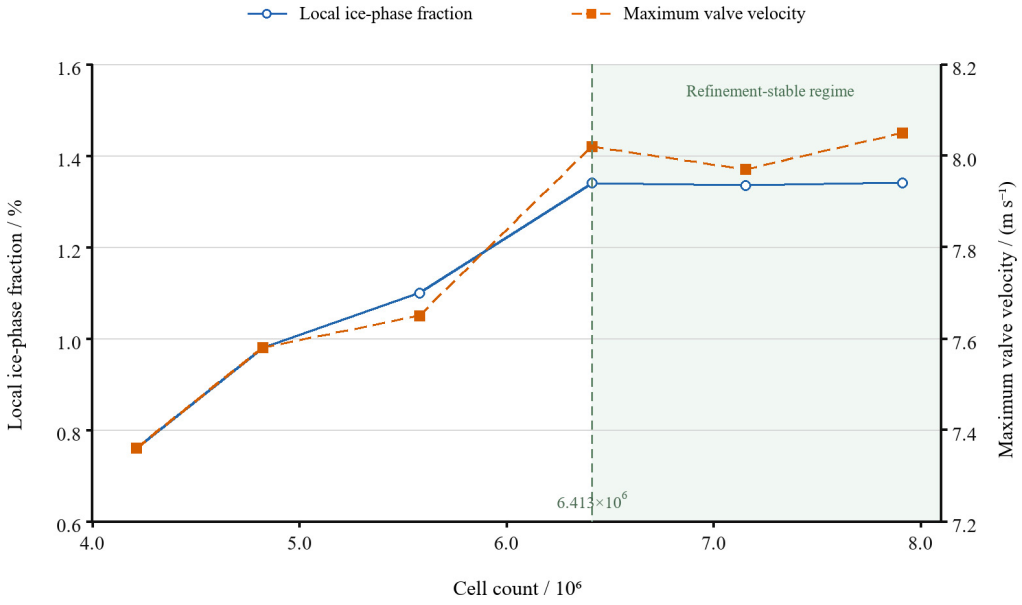


Figure 7. Effects of cell count on the local ice-phase fraction in regions A and B and the maximum velocity within the valve.

Further refinement beyond approximately 6.41 million cells produced smaller changes in both metrics. The local ice-phase fractions were 1.340%, 1.335%, and 1.341% for 6,413,254, 7,154,378, and 7,913,146 cells, respectively. The corresponding maximum velocities were 8.02, 7.97, and 8.05 m·s⁻¹. Relative to the finest mesh, the differences for the 6.41-million-cell mesh were 0.075% and 0.373%, respectively. The largest adjacent change among the three fine meshes was below 1.01%. The assessed metrics were therefore insensitive to further refinement within this range.

The six-mesh series above is an independent comparison retained from the original manuscript. The archived baseline case contains 2,072,638 computational cells. The original mesh-series comparison does not directly establish mesh independence for this archived grid.

3.4. Boundary Conditions and Numerical Settings

The fluid domain was initially filled with water at 277.15 K (4 °C). Oxygen entered through a mass-flow inlet at 153.15 K (−120 °C). A pressure outlet was prescribed at a gauge pressure of 3.0 × 10⁶ Pa, with an operating pressure of 101,325 Pa. The walls were no-slip and adiabatic.

The inlet mass flow of 0.0010–0.0020 kg·s⁻¹ (1.0–2.0 g·s⁻¹) represents localized entry of a small amount of cold gas through the seat clearance before full disc lift. This stage was represented by a fixed small opening. Mass flow was imposed as an independent boundary condition rather than obtained from coupled valve-motion and supply-system calculations. The functional-test range of 0.67814–0.79061 kg·s⁻¹ describes overboard check-valve discharge capacity at the tested pressure values. The simulations and tests therefore address low-flow cooling and valve functionality, respectively. Because the analysis concerns the initial stage at a small lift, full-discharge operation was not simulated. The present results are not extrapolated to freezing during full discharge.

The inlet flow series comprised 0.0010, 0.0012, 0.0014, 0.0016, 0.0018, and 0.0020 kg·s^{-1} at a fixed equivalent sand-grain roughness of 0.8 μm. The roughness series comprised 0.5, 0.6, 0.7, 0.8, 0.9, and 1.0 μm (5.0 × 10^{-7}–1.0 × 10^{-6} m). Its inlet mass flow rate was fixed at 0.0015 kg·s^{-1}. The roughness constant was C_s = 0.5. Each series varied one parameter while holding the other fixed.

The simulations used the pure-water properties and constant gas properties in Table 5, with adiabatic walls. Volume expansion caused by the density change upon freezing was neglected. This configuration compares initial phase-change responses at a fixed small lift. Geometric contraction, flow turning, and viscous resistance still affect velocity and pressure through the momentum equations. The constant-property approximation does not represent gas-density changes with temperature and pressure or enthalpy–temperature coupling during real-gas throttling.

Gas compressibility must be assessed from local velocity and pressure variation. The Mach number Ma is the ratio of local gas velocity U (m·s^{-1}) to sound speed a (m·s^{-1}). Joule–Thomson cooling depends on the state-dependent coefficient μ_{JT} (K·Pa^{-1}) and local pressure drop Δp (Pa). Neither a low mass flow rate nor a short simulation duration alone establishes that these effects are negligible. An independent thermodynamic estimate using the oxygen equation of state in CoolProp 8.0 distinguished local expansion cooling from discrepancies in reference properties [52,53]. At 153.15 K and a reference absolute pressure of 3.101325 × 10^6 Pa, oxygen density is approximately 105.28 kg·m^{-3}. The sound speed is approximately 205.49 m·s^{-1}, and μ_{JT} is approximately 9.05 × 10^{-6} K·Pa^{-1}. An assumed local pressure drop of 1.0 × 10^4 Pa gives an isenthalpic temperature decrease of approximately 0.09 K. This estimate illustrates the temperature-change scale at a small pressure difference; it does not establish the pressure drop across the simulated valve.

The reference density above is substantially higher than the value of 3.136 kg·m^{-3} actually used in Table 5. At the same inlet mass flow, a density difference changes gas volumetric flow, gas–liquid interface advance, and residence time. A small local expansion-induced temperature decrease therefore does not establish that near-wall freezing trends remain unaffected. The properties actually used by the solver are retained, and the numerical results are restricted to comparisons of initial phase change within the constant-property model. They are not treated as validated freezing predictions for real high-pressure oxygen.

Three-dimensional transient simulations were performed in Ansys Fluent 2022 R1. The governing equations were discretized using the finite-volume method. Pressure–velocity coupling used the pressure-implicit with splitting of operators (PISO) algorithm. The physical time step was 1.0 × 10^{-5} s.

The scaled-residual thresholds were 1.0 × 10^{-3} for continuity, velocity, and turbulence equations and 1.0 × 10^{-6} for energy [51]. The final saved continuity residual in the baseline case was 9.34 × 10^{-4}. The x-, y-, and z-velocity residuals were 1.53 × 10^{-6}, 7.33 × 10^{-7}, and 7.42 × 10^{-7}, respectively. The energy residual was 3.65 × 10^{-7}. The k and ε_t residuals were 1.16 × 10^{-4} and 2.05 × 10^{-4}, respectively.

Figure 8 shows 709 saved scaled-residual records from the baseline case, spanning solver iterations 31,512–36,209. Inner-iteration residuals fluctuated as the transient solution advanced between time steps. The values reported above are those at the end of this saved record.

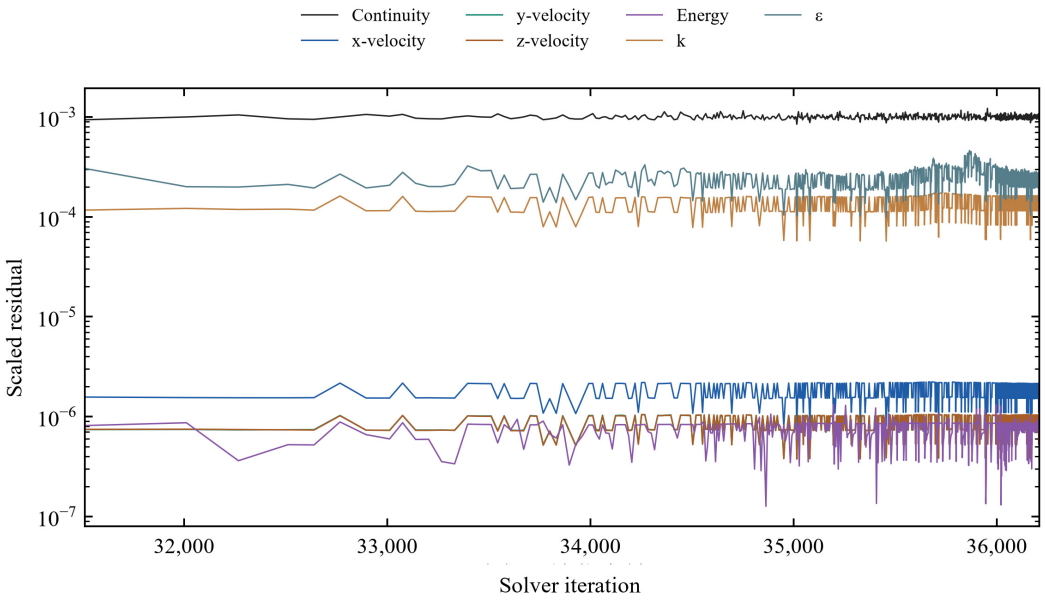


Figure 8. Saved scaled-residual history for the baseline case. The horizontal axis shows solver iteration number; the vertical axis is logarithmic. The y- and z-velocity residual curves largely overlap.

All cases were compared over 0–0.10 s to examine the initial thermal shock and phase-change response after cold gas contacted the water-containing passage. This time marks the endpoint of the statistical analysis. Existing monitoring records beyond 0.10 s supplement the discussion of peaks, declines, and continued growth. Their durations differ among cases, so they are not used to compare long-term limiting ice accumulation.

3.5. Metrics for Transient Freezing Response

The ice-phase fraction is defined as the solid-water volume divided by the volume of the reference domain Ω_{ref}. This domain is the fluid zone named fluid-water, with the same definition used for every case. The metric describes the overall solid-phase level in that domain; it is not the blockage ratio at the minimum valve-seat flow area.

$$\alpha_i(t) = \frac{\sum_{c\in\Omega_{\mathrm{ref}}} \alpha_{l,c}(t)[1-\beta_c(t)]V_c}{\sum_{c\in\Omega_{\mathrm{ref}}} V_c} \tag{16}$$

In Equation (16), c is the cell index, and V_c is cell volume (m³). The water-phase volume fraction $\alpha_{l,c}$ and its internal liquid fraction β_c are dimensionless. The parameter analysis uses whole-domain statistics, defined separately from the local region A and B metrics in Section 3.3.

The local rate of change is calculated by the finite-difference expression

$$r_i(t_j) = \frac{\alpha_i(t_{j+1}) - \alpha_i(t_{j-1})}{t_{j+1} - t_{j-1}} \tag{17}$$

The time-averaged fraction and late-stage rate of change are calculated as

$$\alpha_{i,\mathrm{avg}} = \frac{1}{T}\int_0^T \alpha_i(t)\mathrm{d}t \tag{18}$$

$$(r_{\mathrm{late}}, b^*) = \arg\min_{r,b} \sum_{t_j\in[0.08,0.10]} [\alpha_i(t_j) - (rt_j + b)]^2 \tag{19}$$

In Equation (17), j is the time index, t_j is in s, and r_i is in s⁻¹. In Equation (18), T is the 0.10 s statistical window, and $\alpha_{i,\mathrm{avg}}$ is dimensionless. In Equation (19), r is the late-stage slope (s⁻¹), b is the dimensionless intercept, and the asterisk denotes the least-squares

solution. Each case contains 10,001 recorded time points. Terminal and maximum values and the first time of reaching the maximum were extracted from the complete time series within 0–0.10 s. Time averages were calculated by trapezoidal integration, and late-stage slopes were fitted over 0.08–0.10 s.

Python 3.12 scripts were used for statistical analysis and plotting. Rates were calculated using Equation (17), with uniform 5 ms evaluation intervals in the main analysis. Intervals of 1, 2.5, and 10 ms were also examined to assess interval effects. The time-history plots display time-series points at approximately 5 ms intervals. Shape-preserving piecewise cubic interpolation was used only to draw the trend curves.

The terminal reduction relative to the 0.0010 kg·s^{-1} case is

$$\eta_i = \left(1 - \frac{\alpha_i(T)}{\alpha_{\mathrm{ref}}(T)}\right) \times 100\% \tag{20}$$

For the roughness series, the increase relative to the lowest sampled terminal fraction is

$$\Delta\alpha_i = \left(\frac{\alpha_i(T)}{\alpha_{\min}(T)} - 1\right) \times 100\% \tag{21}$$

In Equations (20) and (21), the reference fractions α_{ref} and $\alpha_{\min}$ are dimensionless. The relative changes η_i and $\Delta\alpha_i$ are expressed as percentages. Statistics were calculated from unrounded data. Ice-phase fractions displayed in the parameter analysis in Section 4 are rounded to two decimal places. A fractional rate of 1 s^{-1} corresponds to 100 percentage points per second.

4. Initial Transient Numerical Results

4.1. Effect of Inlet Mass Flow Rate

The ice-phase fraction generally decreased as inlet mass flow increased, although the response was nonmonotonic (Figure 9). At 0.10 s, it decreased from 0.70% to 0.58% as flow increased from 0.0010 to 0.0012 kg·s^{-1}. It then rose to 0.67% at 0.0014 kg·s^{-1}. Further increases to 0.0016, 0.0018, and 0.0020 kg·s^{-1} yielded terminal fractions of 0.50%, 0.21%, and 0.14%, respectively. At 0.0010–0.0012 kg·s^{-1}, the fraction increased over most of the window, with terminal values close to the maxima within that window.

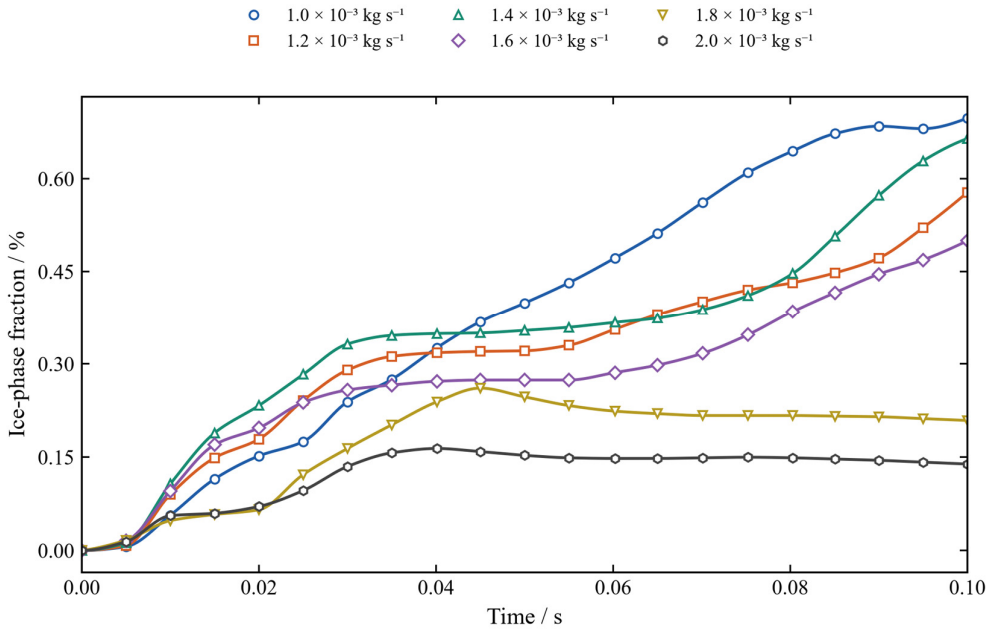


Figure 9. Ice-phase fraction at different inlet mass flow rates. Symbols represent time-series samples; curves are shape-preserving interpolants.

At 0.0016 kg·s^{-1}, the terminal ice-phase fraction was 0.50% and was still increasing late in the window. At 0.0018 and 0.0020 kg·s^{-1}, the fractions first reached their window maxima at approximately 0.04484 and 0.04031 s, respectively. The corresponding maximum fractions were approximately 0.26% and 0.17%. They subsequently declined, ending approximately 20% and 16% below their respective maxima.

Figure 10 shows high-velocity regions within the throttling passage adjacent to low-velocity regions near the stepped geometry. The velocity field was spatially nonuniform at every flow rate examined.

The terminal and time-averaged ice-phase fractions showed similar responses to flow rate (Figure 11 and Table 6). Relative to 0.0010 kg·s^{-1}, terminal reductions at 0.0012, 0.0014, 0.0016, 0.0018, and 0.0020 kg·s^{-1} were 17.2%, 4.7%, 28.4%, 70.1%, and 80.1%, respectively. The time-averaged fraction at 0.0014 kg·s^{-1} also exceeded that at 0.0012 kg·s^{-1}.

Increasing the flow rate from 0.0010 to 0.0020 kg·s^{-1} reduced the time-averaged ice-phase fraction from 0.39% to 0.12%. This reduction of 68.1% was smaller than the 80.1% reduction in the terminal fraction. At the higher mass flows in this series, fractions declined after early accumulation, producing larger differences at the window endpoint than in the time averages.

Over 0.08–0.10 s, the largest positive late-stage slope was 1.153 × 10^{-1} s^{-1} at 0.0014 kg·s^{-1}. The slopes at 0.0018 and 0.0020 kg·s^{-1} were −3.923 × 10^{-3} and −5.316 × 10^{-3} s^{-1}, respectively, indicating declining late-stage fractions.

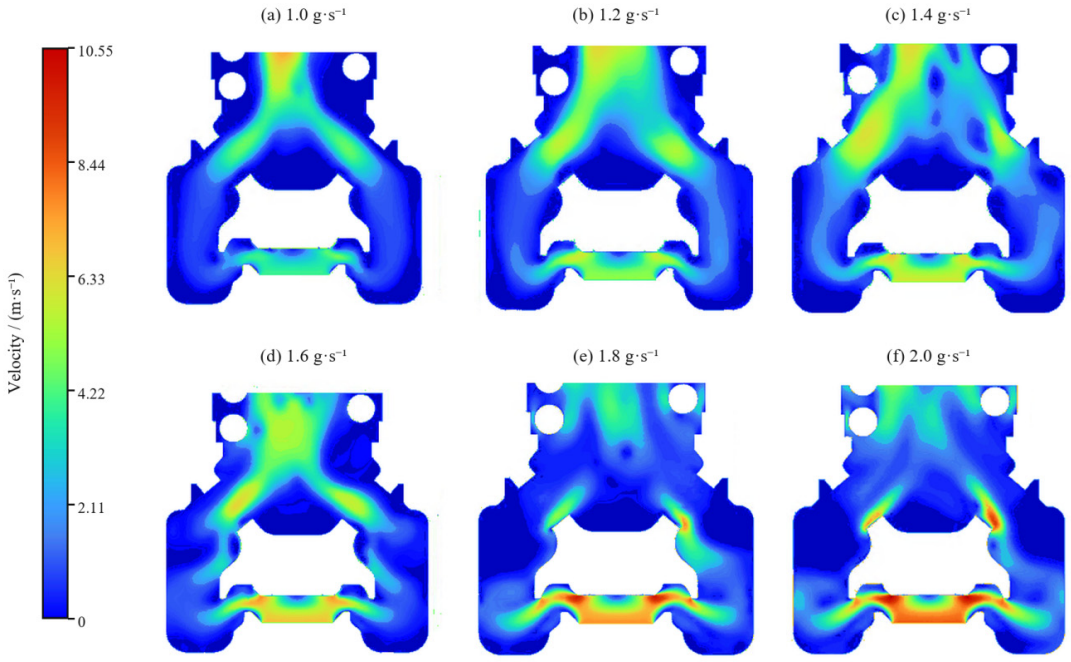


Figure 10. Velocity distributions at different inlet mass flow rates.

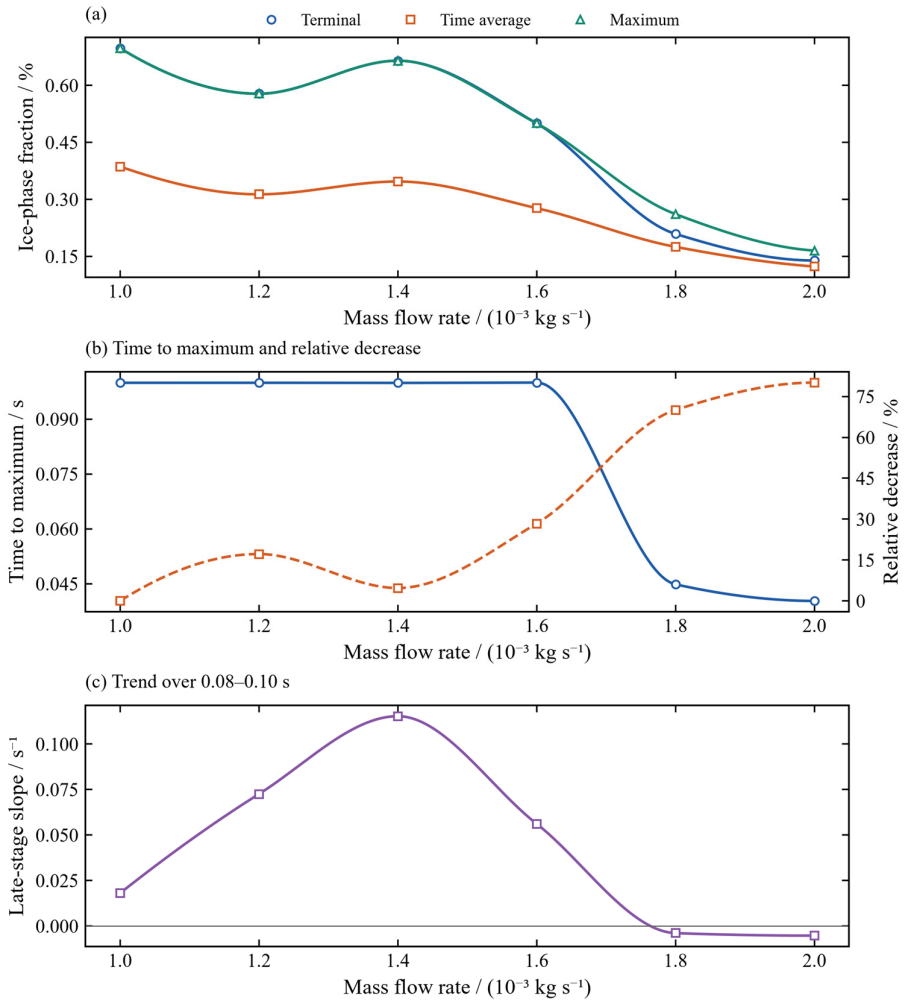


Figure 11. Ice-formation response metrics for the inlet flow-rate series. (**a**) Terminal, time-averaged, and maximum fractions; (**b**) time to maximum and terminal reduction; (**c**) late-stage slope.

Table 6. Ice-phase fraction metrics for the inlet flow-rate series over 0–0.10 s.

Mass Flow Rate kg·s⁻¹ (*g*·s⁻¹)	Terminal, %	Time Average, %	Maximum, %	Late-Stage Slope, s⁻¹
0.0010 (1.0)	0.70	0.39	0.70	1.802×10^{-2}
0.0012 (1.2)	0.58	0.31	0.58	7.252×10^{-2}
0.0014 (1.4)	0.67	0.35	0.67	1.153×10^{-1}
0.0016 (1.6)	0.50	0.28	0.50	5.614×10^{-2}
0.0018 (1.8)	0.21	0.17	0.26	-3.923×10^{-3}
0.0020 (2.0)	0.14	0.12	0.17	-5.316×10^{-3}

Figure 12 compares the wall-area-averaged shear stress at inlet flow rates of 0.0010, 0.0015, and 0.0020 kg·s⁻¹. All three curves decreased rapidly at first and changed more gradually thereafter. The enlarged panel shows their differences near 0.10 s.

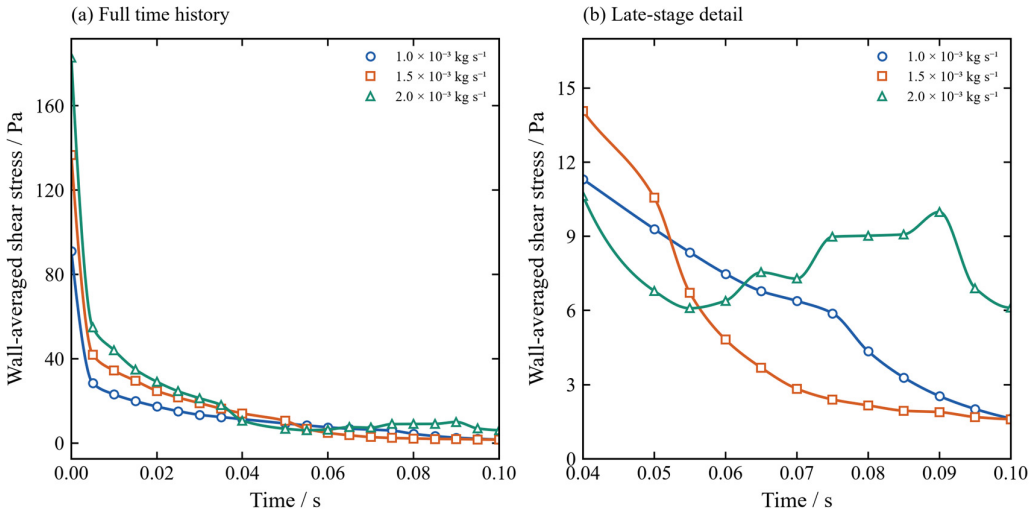


Figure 12. Wall-area-averaged shear stress. (**a**) Full time series; (**b**) enlarged view over 0.04–0.10 s.

At 0.10 s, the three shear stresses were 1.63, 1.60, and 6.11 Pa, respectively. The intermediate flow rate in this series was 0.0015 kg·s^{-1}. It was compared qualitatively with the neighboring conditions of 0.0014 and 0.0016 kg·s^{-1} in the ice-phase fraction series.

The terminal shear stress at 0.0020 kg·s^{-1} was approximately 3.75 times that at 0.0010 kg·s^{-1}. This condition also exhibited a lower ice-phase fraction and a negative late-stage slope.

4.2. Effect of Wall Roughness

The six equivalent sand-grain roughness conditions exhibited a nonmonotonic response (Figure 13). At 0.5 μm, the ice-phase fraction reached 1.37% at approximately 81 ms before declining to 1.34%, which remained higher than all other conditions. Terminal fractions were 0.31% and 0.30% at 0.6 and 0.7 μm, respectively. Further increases in roughness raised the terminal fraction to 0.51%, 0.62%, and 0.64%, respectively.

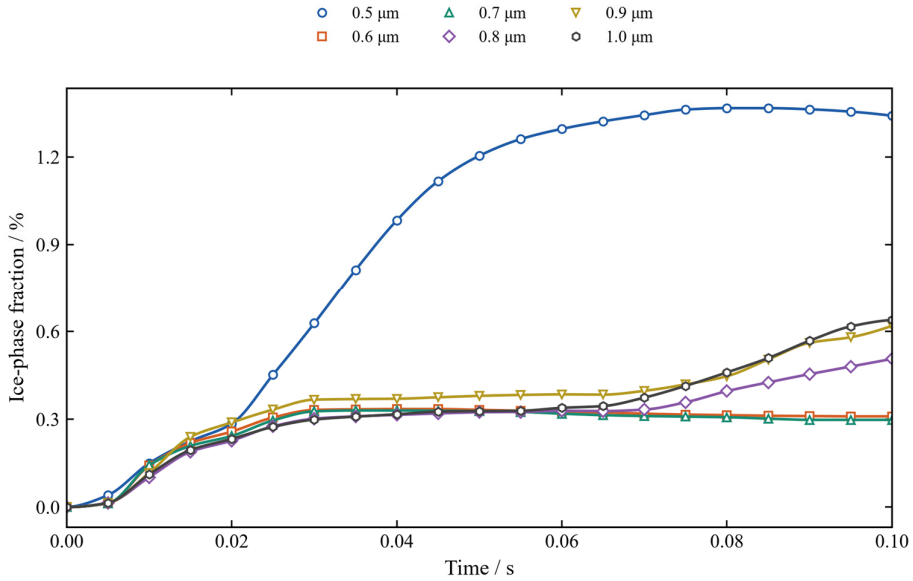


Figure 13. Ice-phase fraction histories at different equivalent sand-grain roughness values.

Ice-accumulation histories also differed among roughness conditions (Figure 14 and Table 7). At 0.6 and 0.7 μm, the fractions reached their window maxima earlier and changed more gradually thereafter. At 0.8–1.0 μm, time-averaged fractions were lower than at 0.5 μm, but the fractions continued increasing late in the window. Their window maxima occurred near 0.10 s.

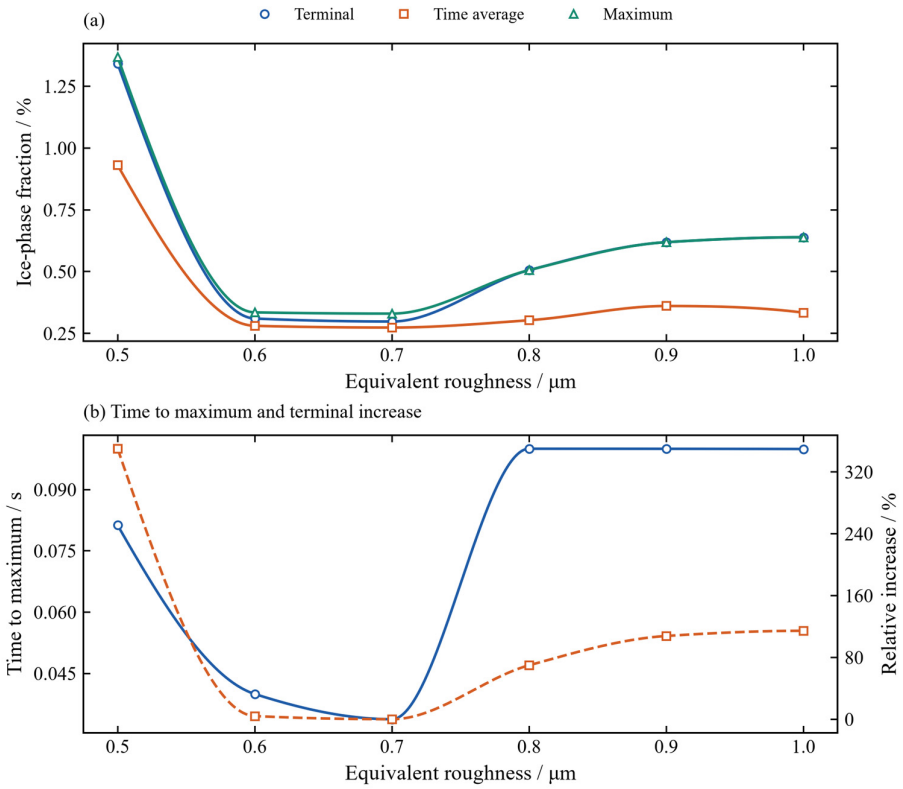


Figure 14. Ice-formation response metrics for the roughness series. (**a**) Terminal, time-averaged, and maximum fractions; (**b**) time to maximum and terminal increase.

Table 7. Ice-phase fraction metrics for the roughness series over 0–0.10 s.

K_s, m (μm)	Terminal, %	Time Average, %	Maximum, %	Late-Stage Slope, s^{-1}
5.0×10^{-7} (0.5)	1.34	0.93	1.37	-1.271×10^{-2}
6.0×10^{-7} (0.6)	0.31	0.28	0.34	-1.970×10^{-3}
7.0×10^{-7} (0.7)	0.30	0.27	0.33	-3.482×10^{-3}
8.0×10^{-7} (0.8)	0.51	0.30	0.51	5.451×10^{-2}
9.0×10^{-7} (0.9)	0.62	0.36	0.62	8.404×10^{-2}
1.0×10^{-6} (1.0)	0.64	0.33	0.64	9.683×10^{-2}

The time-averaged fraction at 0.5 μm was 0.93%, approximately 3.40 times the 0.27% value at 0.7 μm. Calculations using unrounded values showed terminal and time-averaged fractions at 0.6 μm exceeding those at 0.7 μm by 4.0% and 2.6%, respectively.

Figure 15 shows the local turbulent kinetic energy distributions for the roughness series. Peak values at 0.5, 0.6, 0.7, 0.8, 0.9, and 1.0 μm were 7.24, 6.69, 9.32, 5.80, 6.13, and 7.68 $m^2 \cdot s^{-2}$, respectively. Figure 16 compares these peaks with the time-averaged ice-phase fraction over the full domain.

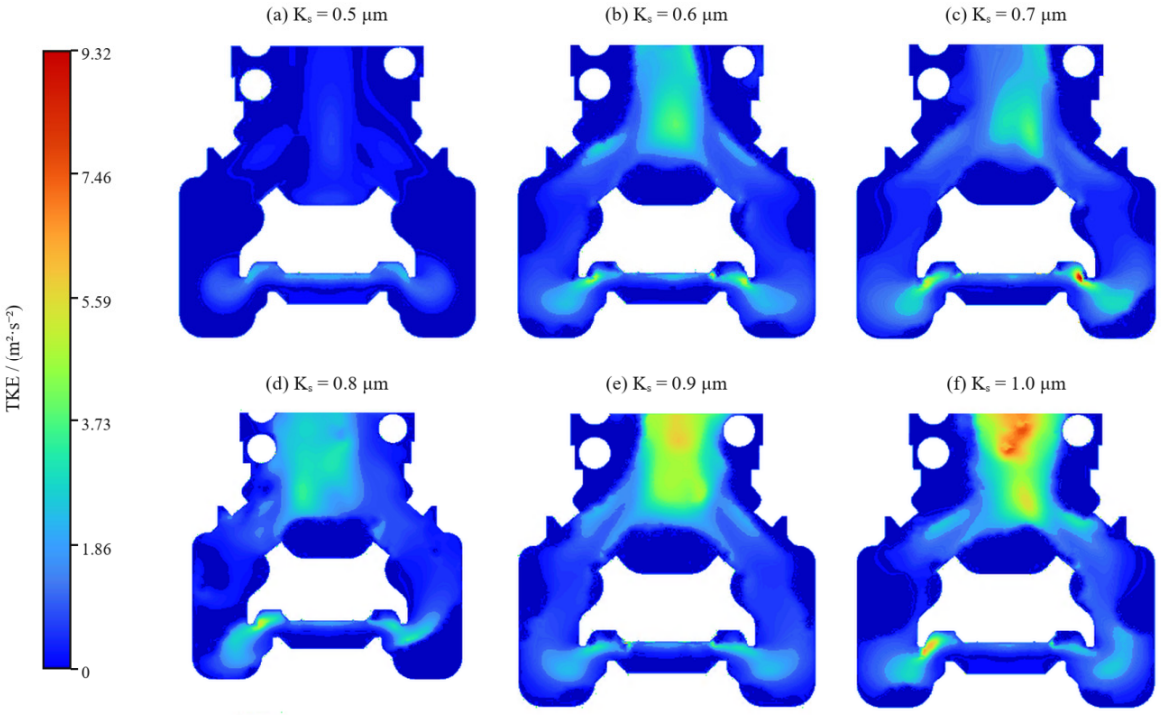


Figure 15. Local turbulent kinetic energy distributions at different equivalent sand-grain roughness values.

The 0.7 μm condition had the highest local turbulent kinetic energy peak and the lowest time-averaged ice-phase fraction. Increasing the roughness to 0.8 μm reduced the kinetic energy peak to 5.80 $m^2 \cdot s^{-2}$ and changed the late-stage ice-phase fraction slope to positive.

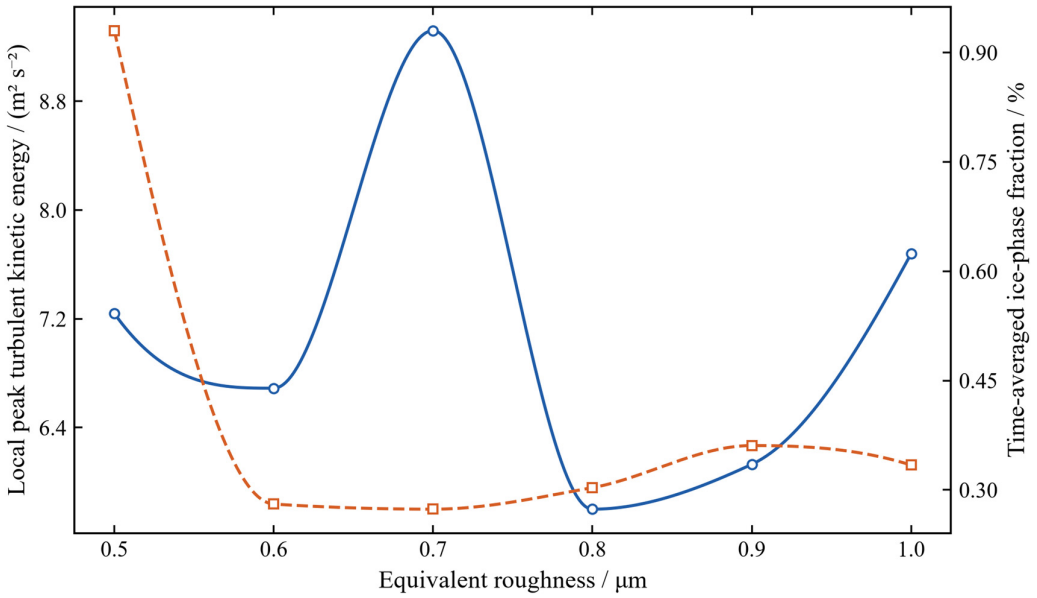


Figure 16. Local peak turbulent kinetic energy and time-averaged ice-phase fraction for the roughness series.

Peak turbulent kinetic energy and time-averaged ice-phase fraction did not consistently vary in opposite directions. At 0.5 μm, the kinetic energy peak was 7.24 $m^2 \cdot s^{-2}$, while the time-averaged ice-phase fraction was the highest. From 0.8 to 1.0 μm, both the kinetic energy peak and terminal ice-phase fraction increased.

Over 0.08–0.10 s, the late-stage slopes at 0.5, 0.6, and 0.7 μm were −0.01271, −0.00197, and −0.00348 s^{-1}, respectively (Figure 17 and Table 7). All three fractions declined, although the solid-phase fraction remained markedly higher at 0.5 μm.

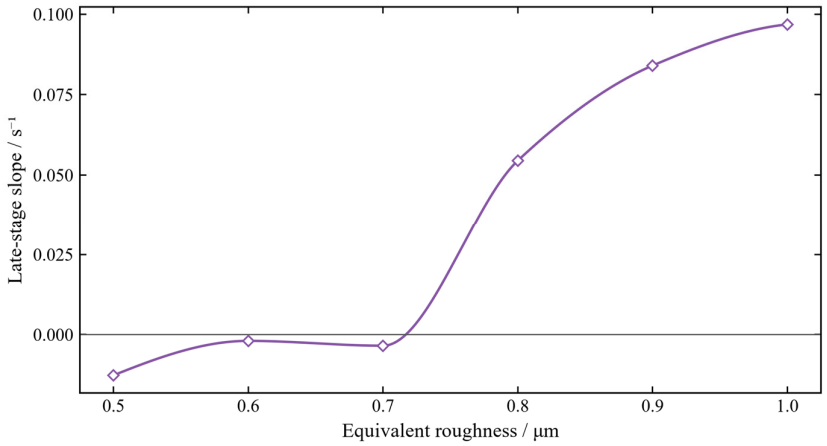


Figure 17. Late-stage slopes at different equivalent sand-grain roughness values, fitted over 0.08–0.10 s.

Late-stage slopes at 0.8, 0.9, and 1.0 μm were 0.05451, 0.08404, and 0.09683 s^{-1}, respectively. Their terminal ice-phase fractions exceeded that at 0.7 μm by 69.8%, 107.7%, and 114.4%, respectively. These conditions had higher solid-phase fractions than the 0.7 μm condition late in the 0–0.10 s window and continued to increase.

4.3. Peak Growth Rate and Effect of the Evaluation Interval

Figure 18 presents the peak rates of change and their occurrence times for each condition, evaluated at a 5 ms interval.

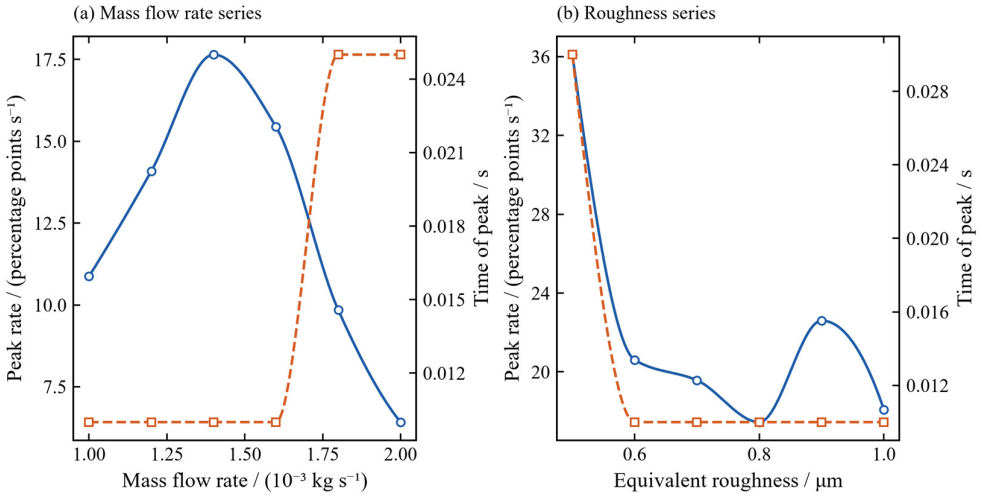


Figure 18. Peak central-difference rates of change and their occurrence times at a 5 ms evaluation interval. Blue circles and solid curves indicate peak rates (left axes); orange squares and dashed curves indicate the times of these peaks (right axes).

https://doi.org/10.3390/jmse14212042

The highest peak rate in the flow-rate series was 17.65 percentage points·s^{-1} at 0.0014 kg·s^{-1}, occurring at approximately 0.010 s. Peak rates at 0.0016, 0.0018, and 0.0020 kg·s^{-1} were 15.44, 9.85, and 6.42 percentage points·s^{-1}, respectively. The latter two peaked at approximately 0.025 s. Under all these conditions, the rate peaked before the ice-phase fraction reached its maximum.

In the roughness series, the 0.5 μm condition reached 36.10 percentage points·s^{-1} at 30 ms. The 0.7 μm condition reached 19.57 percentage points·s^{-1} at 10 ms, while the 0.9 μm condition peaked at 22.60 percentage points·s^{-1}. At 0.8 μm, the peak was 17.45 percentage points·s^{-1}, lower than at 0.7 μm. Nevertheless, its terminal ice-phase fraction was higher and its late-stage slope remained positive. A lower peak rate therefore did not necessarily correspond to a lower solid-phase fraction.

The peak rates varied with the evaluation interval (Figure 19). At 0.0014 kg·s^{-1}, intervals of 1, 2.5, and 5 ms yielded peaks of 22.75, 21.49, and 17.65 percentage points·s^{-1}, respectively. At 0.0020 kg·s^{-1}, the corresponding peaks were 12.55, 8.94, and 6.42 percentage points·s^{-1}. The peak times also changed with the evaluation interval.

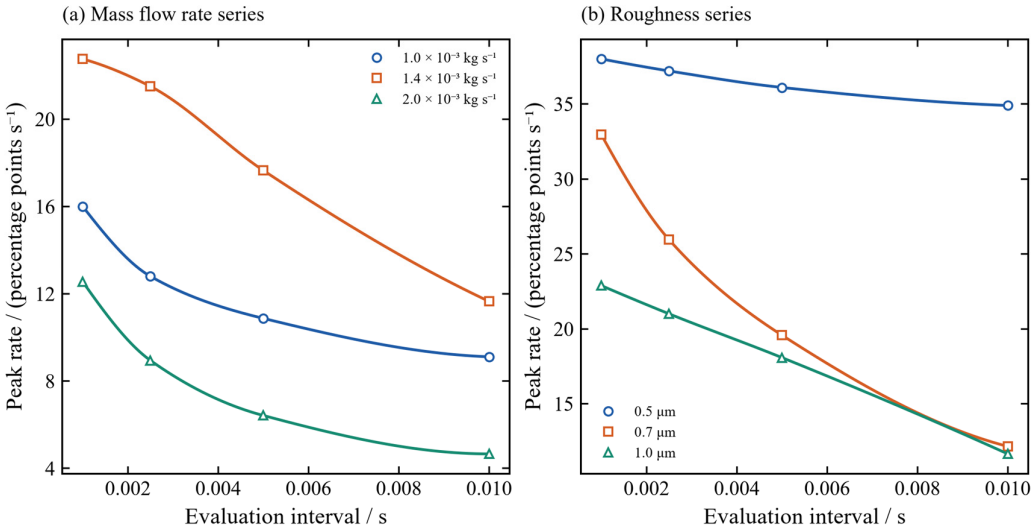


Figure 19. Dependence of peak rate of change on the post-processing evaluation interval.

Sensitivity to the evaluation interval also differed among roughness conditions. At 0.5 μm, the three intervals yielded peaks of 38.00, 37.20, and 36.10 percentage points·s^{-1}, respectively. At 0.7 μm, the corresponding peaks were 32.95, 25.95, and 19.57 percentage points·s^{-1}. Both peak magnitude and occurrence time should therefore be reported together with the evaluation interval. A 5 ms interval was used consistently for comparisons among conditions in this study.

4.4. Comparison of Flow-Rate and Roughness Effects

Figure 20 compares relative changes in the two parameter series, referenced to 0.0010 kg·s^{-1} and 0.7 μm, respectively. At the higher flow rates in this series, terminal reductions exceeded reductions in the time averages. At 0.5 μm, the terminal fraction exceeded its reference value by 350.0%, while the time-averaged fraction was approximately 240.0% higher.

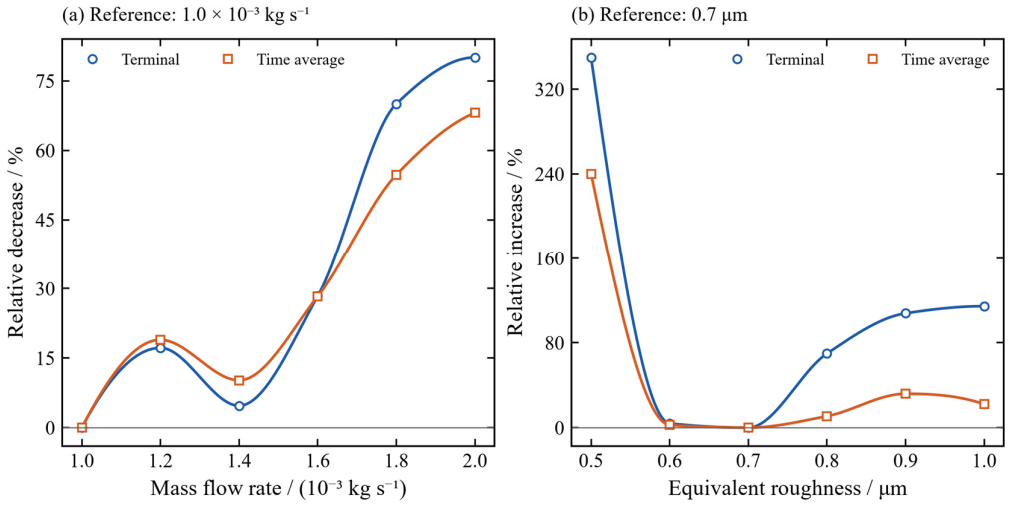


Figure 20. Relative changes in terminal and time-averaged ice-phase fractions. Each panel uses the reference condition for its respective parameter series.

Each parameter series held the other parameter constant, and the reference values and parameter ranges differed. Figure 20 therefore compares relative changes within each series. Comparing overall sensitivity to flow rate and roughness requires a common basis for the parameter ranges.

5. Discussion

Changes in flow rate affect cooling input, water-phase transport, and near-wall momentum exchange simultaneously. The local rise at intermediate flow rates and post-peak decline at higher rates show a stage-dependent, nonmonotonic relationship between ice-phase fraction and inlet flow. Previous studies likewise found that flow affects heat transport at the phase interface, while interface evolution alters the local flow [4–10,17–27]. The spatially nonuniform velocity and differences in turbulent kinetic energy observed here reflect this coupling. Local temperature and interface information are still needed to resolve the contributions of individual heat-transfer processes.

The terminal ice-phase fraction at 0.10 s describes the solid-phase level at the end of the initial comparison window. The time average and late-stage slope add information about earlier accumulation and the final trend, respectively. Despite declining late in this window, the 0.5 μm condition retained a high time-averaged fraction; the fractions at 0.8–1.0 μm continued to increase. A post-peak decline therefore indicates a reduction in solid-phase fraction for a particular condition and interval. It does not establish complete freezing, long-term stability, or elimination of blockage risk.

Existing monitoring records beyond 0.10 s show that growth transitions did not occur simultaneously in all cases. At 0.0012 kg·s^{-1}, the fraction increased from 0.58% at 0.10 s to 1.15% at approximately 0.179 s, then changed little up to 0.20 s. At 0.0014 kg·s^{-1}, it increased from 0.67% at 0.10 s to 1.45% at approximately 0.262 s and then decreased slightly to 1.43% at 0.288 s. By contrast, at 0.0018 kg·s^{-1}, it continued declining from 0.21% at 0.10 s to 0.19% at approximately 0.132 s. For a roughness of 0.9 μm, the fraction increased from 0.62% at 0.10 s to 1.06% at approximately 0.175 s. Its final recorded value remained above the value at the comparison-window endpoint. Some conditions thus reached a plateau or declined after growth, whereas others continued accumulating ice within the available records. The time of 0.10 s provides a common initial comparison point, but it cannot be treated as a common cessation time for freezing in all cases.

Equivalent sand-grain roughness values of 0.6–0.7 μm yielded lower terminal and time-averaged fractions among the discrete conditions examined. Selecting a practical surface also requires consideration of wettability, microstructure, and material effects on ice adhesion [28–37]. Higher wall shear stress coincided with a declining solid-phase fraction, indicating an association between near-wall momentum exchange and phase-change evolution. However, the model did not represent ice adhesion or fracture, so this association does not establish mechanical ice shedding.

Compressed-air tests evaluated prototype opening and discharge under the test conditions. Numerical calculations described initial phase change at a fixed small lift under the specified properties and boundary conditions. The two components address valve functionality and cooling of water-containing passages separately; functional tests cannot quantify errors in the predicted ice-phase fraction. Water temperature, salinity, inlet gas state, and outlet back pressure differ among sea areas and affect freezing [1–5,20,27,46]. Local operating conditions should be expressed as the corresponding flow and thermal boundary conditions. Because the prescribed gas properties differ from those of real high-pressure oxygen, the parameter rankings and ice-phase fractions cannot yet support quantitative predictions for actual operation. Future work should use compatible property and phase-change models, incorporating salinity transport and conjugate heat transfer through the valve body. Ice-thickness and flow-capacity measurements would also help examine freezing over longer timescales.

6. Conclusions

Compressed-air functional tests assessed the opening and discharge performance of an overboard discharge valve. Simulations examined initial freezing over 0–0.10 s at a fixed small lift with constant properties. The conclusions are as follows.

(1) The overboard discharge assembly opened at 1.53×10^6 Pa, and both check valves opened at 6.50×10^5 Pa. Over 3.55×10^6–3.75×10^6 Pa, the overboard check-valve mass flow rate increased from 0.67814 to 0.79061 kg·s^{-1}, a rise of 16.6%. Discharge varied approximately linearly with pressure over the tested interval for each valve type, supporting the prototype's basic opening and discharge functions.

(2) Under the prescribed numerical boundaries and property assumptions, increasing inlet flow from 0.0010 to 0.0020 kg·s^{-1} reduced the fraction at 0.10 s from 0.70% to 0.14%. The time-averaged fraction decreased from 0.39% to 0.12%, with a local rise at the intermediate flow rate of 0.0014 kg·s^{-1}. At 0.0018 and 0.0020 kg·s^{-1}, fractions declined after their peaks, showing the stage-dependent initial response of the low-flow conditions examined. This result does not establish that freezing is absent during full-discharge operation.

(3) Over 0–0.10 s, terminal ice-phase fractions at equivalent roughness of 0.6 and 0.7 μm were 0.31% and 0.30%, respectively, below the other values examined. The 0.5 μm condition had a higher time-averaged fraction, whereas fractions at 0.8–1.0 μm continued increasing late in the window. Combining terminal fraction, time average, and late-stage slope distinguishes higher average solid-phase levels from continued growth near the window endpoint. These conclusions concern initial phase change within the present model. They do not determine long-term steady ice accumulation, time to complete blockage, or safe operating limits for the actual valve.

Author Contributions: Conceptualization, P.L. and Y.S.; methodology, P.L., S.Z., X.Z., C.L., X.L. and Y.S.; software, S.Z. and Z.X.; validation, P.L., C.L. and X.L.; formal analysis, S.Z., X.Z., C.L., X.L. and Z.X.; investigation, P.L., X.Z. and X.L.; resources, P.L. and X.L.; data curation, P.L., S.Z. and Z.X.; writing—original draft preparation, X.Z. and Z.X.; writing—review and editing, P.L., X.L., Z.X.

and Y.S.; visualization, S.Z. and Z.X.; supervision, Y.S.; project administration, P.L. and Y.S. All authors have read and agreed to the published version of the manuscript.

Funding: This work was financially supported by the Project of Simulation Analysis of Sea-crossing Components (MK240701-01). The APC was funded by the same project.

Data Availability Statement: The data supporting the findings of this study are not publicly available.

Conflicts of Interest: The authors declare no conflict of interest.

References

1. Li, S.; Lin, B.; Bai, X.; Wei, P.; Wang, L.; Zhang, R. Numerical Analysis of the Influence of Frost Layers on the Heat Transfer Characteristics of Cryogenic Valves for Polar LNG Ships. *Energies* **2025**, *18*, 302. https://doi.org/10.3390/en18020302.
2. Deshpande, S.; Sundsbø, P.A. Investigation into Using CFD for Estimation of Ship Specific Parameters for the SPICE Model for Prediction of Sea Spray Icing: Part 1—The Proposal. *J. Mar. Sci. Eng.* **2024**, *12*, 1872. https://doi.org/10.3390/jmse12101872.
3. Shi, K.; Duan, X. A Review of Ice Protection Techniques for Structures in the Arctic and Offshore Harsh Environments. *J. Offshore Mech. Arct. Eng.* **2021**, *143*, 064502. https://doi.org/10.1115/1.4050893.
4. Du, Y.; Calzavarini, E.; Sun, C. The physics of freezing and melting in the presence of flows. *Nat. Rev. Phys.* **2024**, *6*, 676-690. https://doi.org/10.1038/s42254-024-00766-5.
5. Du, Y.; Wang, Z.; Jiang, L.; Calzavarini, E.; Sun, C. Sea water freezing modes in a natural convection system. *J. Fluid Mech.* **2023**, *960*, A35. https://doi.org/10.1017/jfm.2023.215.
6. Wang, Z.; Calzavarini, E.; Sun, C.; Toschi, F. How the growth of ice depends on the fluid dynamics underneath. *Proc. Natl. Acad. Sci. USA* **2021**, *118*, e2012870118. https://doi.org/10.1073/pnas.2012870118.
7. Wang, Z.; Jiang, L.; Du, Y.; Sun, C.; Calzavarini, E. Ice front shaping by upward convective current. *Phys. Rev. Fluids* **2021**, *6*, L091501. https://doi.org/10.1103/physrevfluids.6.l091501.
8. Couston, L.A.; Hester, E.; Favier, B.; Taylor, J.R.; Holland, P.R.; Jenkins, A. Topography generation by melting and freezing in a turbulent shear flow. *J. Fluid Mech.* **2021**, *911*, A44. https://doi.org/10.1017/jfm.2020.1064.
9. Yang, R.; Chong, K.L.; Liu, H.R.; Verzicco, R.; Lohse, D. Abrupt transition from slow to fast melting of ice. *Phys. Rev. Fluids* **2022**, *7*, 083503. https://doi.org/10.1103/physrevfluids.7.083503.
10. Yang, R.; Howland, C.J.; Liu, H.R.; Verzicco, R.; Lohse, D. Ice melting in salty water: Layering and non-monotonic dependence on the mean salinity. *J. Fluid Mech.* **2023**, *969*, R2. https://doi.org/10.1017/jfm.2023.582.
11. Song, J.; Zhang, D.; Yuan, H.; Zhang, J.; Zhou, P.; Li, Y.; Wang, K.; Mei, N. Sea water frozen crystalisation impacted by flow and heterogeneous nucleation: PFM-LBM coupled modeling, simulation and experiments. *Desalination* **2022**, *524*, 115484. https://doi.org/10.1016/j.desal.2021.115484.
12. Krishnaswamy, S.; Sahu, P.; Ponnani, K. Calorimetry based temperature and specific enthalpy measurements associated with ice-water phase change in saline systems for freeze desalination. *Int. J. Thermofluids* **2022**, *15*, 100175. https://doi.org/10.1016/j.ijft.2022.100175.
13. Zhao, C.; Lin, Y.; Wu, X.; Zhang, X.; Chu, F. Nanoscale insights on the freezing front propagation and ion behaviors during seawater freezing. *Appl. Surf. Sci.* **2023**, *641*, 158499. https://doi.org/10.1016/j.apsusc.2023.158499.
14. Wang, Z.; Deng, Z.; Wang, Y.; Yi, Y. Simulation Study on the Factors Affecting the Solidification of Liquid Droplets with Different Salinity on Cold Surfaces. *Appl. Sci.* **2023**, *13*, 994. https://doi.org/10.3390/app13020994.
15. Zhang, Y.; Zhou, X.; Shi, W.; Chi, J.; Li, Y.; Guo, W. A Visualization Experiment on Icing Characteristics of a Saline Water Droplet on the Surface of an Aluminum Plate. *Coatings* **2024**, *14*, 155. https://doi.org/10.3390/coatings14020155.
16. Chu, F.; Li, S.; Zhao, C.; Feng, Y.; Lin, Y.; Wu, X.; Yan, X.; Miljkovic, N. Interfacial ice sprouting during salty water droplet freezing. *Nat. Commun.* **2024**, *15*, 2249. https://doi.org/10.1038/s41467-024-46518-y.
17. Lyu, S.; Wang, K.; Zhang, Z.; Pedrono, A.; Sun, C.; Legendre, D. A hybrid VOF-IBM method for the simulation of freezing liquid films and freezing drops. *J. Comput. Phys.* **2021**, *432*, 110160. https://doi.org/10.1016/j.jcp.2021.110160.
18. Chen, G.; Xia, H.; Bai, X.; Wu, D.; Lin, B. Numerical Analysis of Impact-Freezing and Spreading Dynamics of Supercooled Saline Droplets on Offshore Wind Turbine Blades Using the VOF–Enthalpy–Porosity Method. *J. Mar. Sci. Eng.* **2025**, *13*, 2093. https://doi.org/10.3390/jmse13112093.

19. Wang, Y.; Ju, L.; Han, D.; Wang, Q. Numerical investigation of the impacting and freezing process of a single supercooled water droplet. *Phys. Fluids* **2021**, *33*, 042114. https://doi.org/10.1063/5.0048206.
20. Wan, L.; Liu, X.; Chu, S.; Wang, M.; Wang, Z.; Wang, Y.; Sun, H. Freezing characters study of the sessile seawater drop on a cold substrate. *AIP Adv.* **2023**, *13*, 035021. https://doi.org/10.1063/5.0133949.
21. Lyu, S.; Zhu, X.; Legendre, D.; Sun, C. Liquid encapsulation in a freezing sessile drop. *Droplet* **2023**, *2*, e90. https://doi.org/10.1002/dro2.90.
22. Hou, J.; Gong, J.; Wu, X.; Huang, Q. Numerical study on impacting-freezing process of the droplet on a lateral moving cold superhydrophobic surface. *Int. J. Heat Mass Transf.* **2022**, *183*, 122044. https://doi.org/10.1016/j.ijheatmasstransfer.2021.122044.
23. Wang, Y.; Wang, Q.; Ju, L.; Xue, Y.; Jing, C.; Lu, Y.; Sun, N. Numerical investigation of VOSET and Enthalpy-Porosity method-based freezing process of a supercooled water droplet impacting an isolated vertical plate. *Int. Commun. Heat Mass Transf.* **2025**, *161*, 108400. https://doi.org/10.1016/j.icheatmasstransfer.2024.108400.
24. Li, Y.; Wu, X.; Hou, H.; Chu, F.; Hu, Z. Dynamics and heat transfer of saltwater droplets impact on cold superhydrophobic surfaces. *Int. J. Heat Mass Transf.* **2025**, *249*, 127241. https://doi.org/10.1016/j.ijheatmasstransfer.2025.127241.
25. Zhang, X.; Li, K.; Zhu, Z.; Fang, W.Z.; Zhu, F.Q.; Yang, C. Droplet impact and freezing dynamics on ultra-cold surfaces: A scaling analysis of central-concave pattern. *Appl. Therm. Eng.* **2024**, *239*, 122135. https://doi.org/10.1016/j.applthermaleng.2023.122135.
26. Li, W.; Wang, J.; Tian, L.; Zhu, C.; Zhao, N. Numerical investigation on rebound dynamics of supercooled water droplet on cold superhydrophobic surface. *Appl. Therm. Eng.* **2024**, *239*, 122007. https://doi.org/10.1016/j.applthermaleng.2023.122007.
27. Fan, Y.; Peng, B.; Jiang, P.; Ren, J.; Lin, Y.; Gao, L.; Li, B. Seawater Flow-Freezing Characteristics in Open Container Injection Under Low-Temperature Conditions. *J. Mar. Sci. Eng.* **2025**, *13*, 2289. https://doi.org/10.3390/jmse13122289.
28. Memon, H.; Wang, J.; Hou, X. Interdependence of Surface Roughness on Icephobic Performance: A Review. *Materials* **2023**, *16*, 4607. https://doi.org/10.3390/ma16134607.
29. Dhyani, A.; Choi, W.; Golovin, K.; Tuteja, A. Surface design strategies for mitigating ice and snow accretion. *Matter* **2022**, *5*, 1423-1454. https://doi.org/10.1016/j.matt.2022.04.012.
30. Liu, Y.; Wu, Y.; Liu, S.; Zhou, F. Material Strategies for Ice Accretion Prevention and Easy Removal. *ACS Mater. Lett.* **2022**, *4*, 246-262. https://doi.org/10.1021/acsmaterialslett.1c00365.
31. Rehfeld, N.; Speckmann, B.; Stenzel, V. Parameter Study for the Ice Adhesion Centrifuge Test. *Appl. Sci.* **2022**, *12*, 1583. https://doi.org/10.3390/app12031583.
32. Schneeberger, G.M.; Kozlowski, R.; Wolfe, D.; Palacios, J.L. Development of a durable ice protective coating for use on rotorcraft. *Cold Reg. Sci. Technol.* **2022**, *193*, 103427. https://doi.org/10.1016/j.coldregions.2021.103427.
33. Smith, J.G.; Wohl, C.J.; Palacios, J.L.; Connelly, B.D.; Culver, G.F.; Torchia, P.J.; Chauby, M.J.; Denkins, M.H.; Beck, D.M. Impact ice adhesion strength of stainless steel 304 as determined on a centrifuge test stand. *Cold Reg. Sci. Technol.* **2022**, *196*, 103492. https://doi.org/10.1016/j.coldregions.2022.103492.
34. Farahani, E.; Liberati, A.C.; Mahdavi, A.; Stoyanov, P.; Moreau, C.; Dolatabadi, A. Ice Adhesion Evaluation of PTFE Solid Lubricant Film Applied on TiO2 Coatings. *Coatings* **2023**, *13*, 1049. https://doi.org/10.3390/coatings13061049.
35. Memon, H.; Mirshahidi, K.; Zarasvand, K.A.; Golovin, K.; De Focatiis, D.S.A.; Choi, K.S.; Hou, X. Comparative study on the influence of surface characteristics on de-icing evaluation. *J. Mater. Sci.* **2021**, *56*, 17337–17352. https://doi.org/10.1007/s10853-021-06407-x.
36. Wang, L.; Tian, Z.; Jiang, G.; Luo, X.; Chen, C.; Hu, X.; Zhang, H.; Zhong, M. Spontaneous dewetting transitions of droplets during icing & melting cycle. *Nat. Commun.* **2022**, *13*, 378. https://doi.org/10.1038/s41467-022-28036-x.
37. Huang, W.; Huang, J.; Guo, Z.; Liu, W. Icephobic/anti-icing properties of superhydrophobic surfaces. *Adv. Colloid Interface Sci.* **2022**, *304*, 102658. https://doi.org/10.1016/j.cis.2022.102658.
38. Cai, L.; Mi, S.; Luo, C.; Liu, Z. Numerical investigation of hydraulic and heat transfer characteristics of two-phase ice slurry in helically coiled tubes. *Energy Build.* **2022**, *256*, 111773. https://doi.org/10.1016/j.enbuild.2021.111773.
39. Yang, R.; Howland, C.J.; Liu, H.R.; Verzicco, R.; Lohse, D. Shape effect on solid melting in flowing liquid. *J. Fluid Mech.* **2024**, *980*, R1. https://doi.org/10.1017/jfm.2023.1080.
40. Wang, L.; Wang, J.; Huang, X.; Shangguan, S.; Mao, H.; Li, Y.; Lei, G. Experimental investigation on cryogenic chilldown performance under high-Reynolds number condition and using interior micro-fin structure. *Int. J. Heat Mass Transf.* **2022**, *182*, 121979. https://doi.org/10.1016/j.ijheatmasstransfer.2021.121979.
41. Kim, S.; Foster, D.; Damle, N.; Mudawar, I.; Hartwig, J. Experimental investigation of flow orientation effects on cryogenic flow boiling. *Int. J. Heat Mass Transf.* **2024**, *220*, 124940. https://doi.org/10.1016/j.ijheatmasstransfer.2023.124940.

42. Tao, Z.; Liu, S.; Lu, T.J. Themo-mechanical analysis of a freezing water-filled capillary tube. *Int. J. Heat Mass Transf.* **2024**, *231*, 125782. https://doi.org/10.1016/j.ijheatmasstransfer.2024.125782.
43. Bieder, U.; Herbette, A. CFD analysis of water vapor condensation in large containments: Numerical model, verification and validation. *Nucl. Eng. Des.* **2022**, *395*, 111861. https://doi.org/10.1016/j.nucengdes.2022.111861.
44. Xue, W.; Wang, H.; Roy, C.J. Code Verification for the SENSEI CFD Code. *J. Verif. Valid. Uncertain. Quantif.* **2023**, *8*, 021003. https://doi.org/10.1115/1.4062609.
45. Li, Y.; Liu, Y. A Mathematical Model of Heat Transfer in Problems of Pipeline Plugging Agent Freezing Induced by Liquid Nitrogen. *Fluid Dyn. Mater. Process.* **2022**, *18*, 775-788. https://doi.org/10.32604/fdmp.2022.019810.
46. Martini, F.; Contreras Montoya, L.T.; Ilinca, A. Review of Wind Turbine Icing Modelling Approaches. *Energies* **2021**, *14*, 5207. https://doi.org/10.3390/en14165207.
47. Toppaladoddi, S. Nonlinear interactions between an unstably stratified shear flow and a phase boundary. *J. Fluid Mech.* **2021**, *919*, A28. https://doi.org/10.1017/jfm.2021.396.
48. GB/T 12241—2021; Safety Valves—General Requirements. Standards Press of China: Beijing, China, 2021. (In Chinese)
49. Hefei General Mechanical and Electrical Products Inspection Institute Co., Ltd. *Test Report 2026FM099: Overboard Discharge Valve Assembly and Check Valves*; ZD092BT-024-54; Hefei General Mechanical and Electrical Products Inspection Institute Co., Ltd.: Hefei, China; 8 March 2026; pp. 1–5. (In Chinese)
50. Yang, H.; Jiang, D. Research on Oxygenation Components under a High-Pressure Oxygen Environment. *Appl. Sci.* **2023**, *13*, 7703. https://doi.org/10.3390/app13137703.
51. Ansys. Ansys Fluent Theory Guide and User's Guide, Release 2024 R2. Available online: https://ansyshelp.ansys.com/public/Views/Secured/corp/v242/en/flu_th/flu_th.html (accessed on 15 October 2026).
52. Bell, I.H.; Wronski, J.; Quoilin, S.; Lemort, V. Pure and Pseudo-pure Fluid Thermophysical Property Evaluation and the Open-Source Thermophysical Property Library CoolProp. *Ind. Eng. Chem. Res.* **2014**, *53*, 2498–2508. https://doi.org/10.1021/ie4033999.
53. Schmidt, R.; Wagner, W. A New Form of the Equation of State for Pure Substances and Its Application to Oxygen. *Fluid Phase Equilibria* **1985**, *19*, 175–200. https://doi.org/10.1016/0378-3812(85)87016-3.

Disclaimer/Publisher's Note: The statements, opinions and data contained in all publications are solely those of the individual author(s) and contributor(s) and not of MDPI and/or the editor(s). MDPI and/or the editor(s) disclaim responsibility for any injury to people or property resulting from any ideas, methods, instructions or products referred to in the content.